Journal of Energy Storage 54 (2022) 105277

Contents lists available at ScienceDirect

Journal of Energy Storage

journal homepage: www.elsevier.com/locate/est

Research Papers

Phase change heat transfer and energy storage in a wavy-tube thermal storage unit filled with a nano-enhanced phase change material and metal foams

Mohammad Ghalambaz [a,*], Ammar A. Melaibari [b,c], Ali J. Chamkha [d], Obai Younis [e,f], Mikhail Sheremet [a]

[a] Department of Theoretical Mechanics, Tomsk State University, 36 Lenin Ave., Tomsk 634050, Russia
[b] Mechanical Engineering Department, Faculty of Engineering, King Abdulaziz University, Jeddah 21589, Saudi Arabia
[c] Centre of Nanotechnology, King Abdulaziz University, Jeddah 21589, Saudi Arabia
[d] Faculty of Engineering, Kuwait College of Science and Technology, Doha District, 35004, Kuwait
[e] Department of Mechanical Engineering, College of Engineering at Wadi Addwaser, Prince Sattam Bin Abdulaziz University, Saudi Arabia
[f] Department of Mechanical Engineering, Faculty of Engineering, University of Khartoum, Sudan

ARTICLE INFO

Keywords:
Latent heat thermal energy storage (LHTES)
Nano-enhanced phase change material (NePCM)
Porous medium
Enthalpy-porosity method

ABSTRACT

Latent heat thermal energy storage plays a key role in the thermal management of heat transfer systems, shifting thermal loads, and developing renewable systems. A latent heat thermal energy storage (LHTES) unit can store/release a significant amount of heat in a compact space. However, the main issue of LHTES units is their poor heat transfer characteristics. Thus, the thermal response time of most LHTES is low, and they cannot absorb/release the required energy in a timely manner. Hence, the heat transfer enhancement approaches such as using nano additives, metal foams, and extended, wavy surfaces are promising approaches to improve the heat transfer capability of LHTES. The present study aims to address the impact of using wavy tubes in a composite phase change material and metal foam LHTES unit. A phase change heat transfer model based on enthalpy-porosity was introduced and solved via the finite element approach. The influence of nanoparticle volumetric fraction (VF_{na}), tube wave amplitude (A), tube wave number (N), and the porosity coefficient (ε) was investigated on the charging time, stored energy, and heat transfer behavior of the LHTES unit. According to the findings, employing metal foams and nanoparticles enhances heat transmission and decreases charging time. A simple tube with no wavy surface produces lower pressure drop and better charging power compared to a wavy tube.

1. Introduction

Latent heat thermal energy storage (LHTES) is a promising approach in green energy development. LHTES systems fill the gap between supply and demand time mismatch in solar [1,2] and waste heat recovery [3] applications. LHTES units are compact thermal energy storage components filled with PCM. The PCM sinks/release the thermal energy on phase change at a constant fusion temperature and stores/releases the thermal energy on demand [4,5]. Thus, LHTES acts as a capacitor in a thermal cycle, damping transient load demands, compensating for thermal load mismatches, or providing load shift capabilities [6,7].

PCM can store much energy in a small space with high thermal energy density, but their drawback is the low thermal conductivity and long required time for the charging and discharge process [8]. The low thermal conductivity of PCMs is a heat transfer barrier for the rapid charging or discharging of an LHTES unit on demand. Thus, although an LHTES unit can hold a significant amount of thermal energy to meet a cycle demand, its low heat transfer characteristics cannot adequately regulate a cycle demand.

To increase the heat transfer efficiency of LHTES units, many researchers attempted to promote the heat transfer characteristics of LHTES units by utilizing fins, nano additives, metal foams, close contact melting, extended surfaces, and encapsulation techniques. For example, Arshad et al. [9] employed nanoparticles to enhance the heat transfer of PCMs in a phase change heatsink. The results found that using 1 % copper nanoparticles could optimally enhance the heat transfer rate in

---

[*] Corresponding author.
E-mail address: m.ghalambaz@gmail.com (M. Ghalambaz).

https://doi.org/10.1016/j.est.2022.105277
Received 26 April 2022; Received in revised form 29 June 2022; Accepted 5 July 2022
Available online 13 July 2022

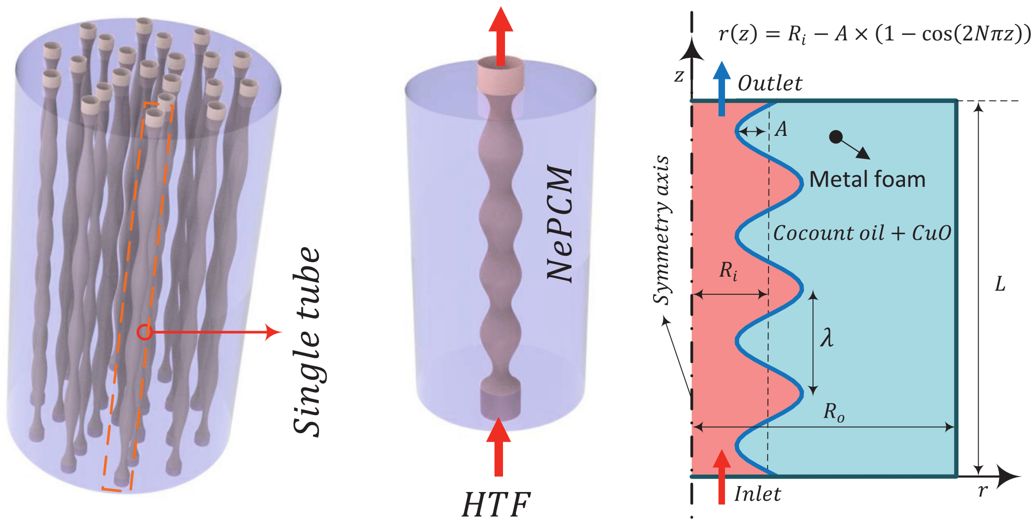

(a) (b) (c)

Fig. 1. The schematic view of the physical model: (a) LHTES unit, (b) single tube with the NEPCM domain, and (3) computational domains.

the heatsink. In another study, Arshad et al. [10] examined the impact of using 0 %–5 % copper nanoparticles embedded in RT-28HC for passive cooling of electronics using PCM-heatsinks. They also showed that using 1 % nanoparticles could optimally promote the heat transfer rate by 1.87 %, with a drawback of a 7.23 % decline in storage capacity. The reduction in storage capacity was since the nanoparticles cannot contribute to latent heat storage. Xu et al. [11] addressed an idea of a cascade of thermal energy storage heat transfer to find an optimal design for thermal energy storage.

Bondareva and Sheremet [12] explored the impact of fins, as a thermal enhancer, in a passive PCM-heatsink. The PCM was embedded in the space between fins, and there was a heat flux source below the heatsink. They considered the natural convection effects in their model. The results showed that the frequency of transient heating loads and the natural convection current could play a major role in the melting behavior of PCM. Al-Najjar et al. [13] utilized a composite layer of PCM-metal foam for heat transfer enhancement in a photovoltaic (PV) solar collector. The authors reported that the average temperature of the PV cell could be declined by 12 °C due to a 127 % improvement in the melting time.

Esapour et al. [14] utilized metal foams as PCM enhancers in a multi-tube LHTES unit. The PCM and metal foam were made of RT35 and copper, respectively. The authors changed the foam porosity between 0.7 and 0.9 could be changed. Using a metal foam with a 0.9 porosity reduced the melting time by 14 %, while a denser foam with a porosity of 0.7 declined the melting time by 55 %. Thus, it can be deduced that the metal foams effectively enhance heat transfer and reduce the melting time (thermal energy storage). Xu et al. [15] examined the impact of porous media on the melting behavior of a PCM in a cavity. They showed that the porous media weakened the natural convection circulations in the cavity.

Some researchers attempted to change the structural shape of an LHTES unit to benefit from a combination of natural convection circulations and thermal conduction. For example, Sardari et al. [16] designed an LHTES air heater, in which an air channel was placed in the middle of a PCM slab while PCM was embedded in a metal foam layer. The airflow could charge/discharge the unit from two sides in this design. Mahdi and Nsofor [17] placed multiple metal foam segments in a horizontal shell-tube LHTES unit with different porosities. Their findings indicated that the energy recovery times could be considerably reduced by employing foam cascading instead of a uniform single segment metal foam. The impact of metal foam [18] or a partial layer of metal foam [19] on heat transfer in tubes was also investigated.

A novel approach that could lead to an improvement in heat transfer is using wavy surfaces. Wavy surfaces increase the length of the heat transfer interface between heat transfer fluids, and hence, they can raise the overall heat transfer rate. However, the waviness of a surface could impact the hydraulic of convection flows and reduce or promote the local heat transfer rate in some regions. Several recent investigations considered wavy surfaces in natural and forced convection applications without phase change heat transfer. The convection heat transfer of nanofluids, viscous fluids, and flow in porous media were addressed in an excellent book by Shenoy et al. [20].

Moreover, Sheremet et al. [21,22], Alsabery et al. [23,24], and Azizul et al. [25] investigated different aspects of natural convection heat transfer in wavy wall enclosures. They concluded that using wavy walls will increase the heat transfer. However, there is an optimum number of undulations in some cases that could maximize the heat transfer. In such studies, the fluid was fully molten, and there was no region involving solid-liquid phase change heat transfer. The behavior of phase change heat transfer in a wavy wall cavity could be completely different from these literature works since there are two separate solid and liquid regions in a LHTES enclosure that evolve over time and shift the hydrodynamic of convection flows.

Only a few studies consider phase change heat transfer and wavy surfaces. Abdollahzadeha and Esmaeilpour [26] investigated the influence of nanoparticle dispersion and surface waviness on the thermal discharging of Cu–water nanofluid in a vertical wavy cavity. The authors revealed that the normal waviness of 0.25 and 0.4 could result in a maximum of 60 % decline in discharging time when the Grashof number is high (i.e., 10^6). Shahsavar et al. [27] utilized a single wavy shell-tube latent heat exchanger. The heat transfer fluid was flowing in a wavy tube while the PCM was inserted in the space between the shell and the tube. The findings indicated that the best configuration of the wavy tube could reduce the melting time by 50 % compared to a smooth design. Ma et al. [28] employed a single passage wavy channel LHTES design for air cooling of a domestic building. These authors also utilized copper oxide nanoparticles and further improved the heat transfer in the thermal storage design.

The literature review indicated a few studies investigating the phase change heat transfer of PCMs in wavy wall enclosures [26–28] in the existence or absence of nano-additives. However, the phase change heat

Table 1
Thermophysical characteristics of the Coconut oil and the nano additives [29,30].

Property	Coconut oil (measured)		Nano additives CuO	HTF (Water)	Copper metal foam
	Solid (15 °C)	Liquid (32 °C)			
ρ_{PCM} (kg m^{-3})	920	914 ± 0.11 %	6500	993.73	8900
μ_{PCM}(Ns m^{-2})	–	0.0326 ± 3 %	–	0.705×10^{-3}	
C_p (J kg^{-1} K^{-1})	3750	2010 ± 0.2 %	540	4178	386
γ (W m^{-1}/K)	0.228	0.166 ± 1.2 %	18	0.623	380
h_f (kJ kg^{-1})		103 ± 1 %	–		
Pr		394.73 ± 3.2 %	–		
T_{me} (°C)	24	–	–	–	–

Table 2
Details of mesh study when $VF_{\text{na}} = 0.02$, $A = 3$ mm, $N = 3$, and $\varepsilon = 0.85$.

Cases	Number of uniform meshes	$MVF\|_{t=2000s}$	Computation time
Case I	75 × 75 × 15	0.8252	8 h 20 min
Case II	100 × 100 × 20	0.7927	13 h 5 min
Case III	**125 × 125 × 25**	**0.7781**	**18 h 15 min**
Case IV	150 × 150 × 30	0.7711	25 h 12 min
Case V	200 × 200 × 40	0.7652	32 h 8 min

The bold row was selected for the computation of the results section.

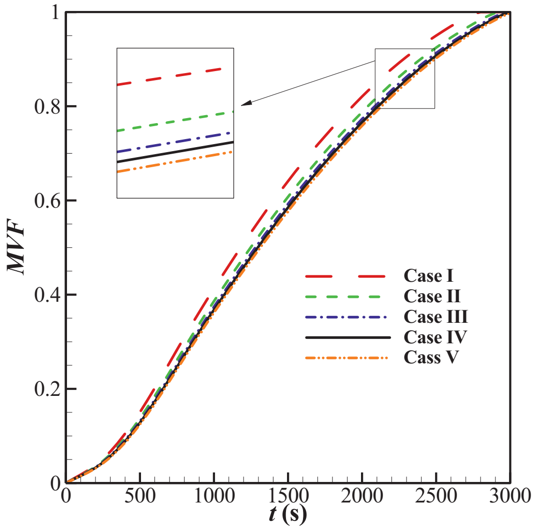

Fig. 2. Impact of grid size on the melting volumetric fraction for case $A = 3$ mm, $N = 3$, $VF_{na} = 0.02$ and $\varepsilon = 0.85$.

transfer of PCMs metal foam composites in wavy wall enclosures have not been addressed yet. The heat transfer behavior of PCMs in metal foam-filled enclosures could be different from clear flow designs [26–28]. In clear flow phase-change heat transfer, there is a poor conduction regime and moderate natural convection circulation, while in composite metal foam PCMs there is a conduction-dominant tendency and poor natural convection flow. Thus, the current research intends to address the thermal energy storage and phase change heat transfer of metal foam composite PCMs with nano additives in wavy wall enclosures for the first time.

2. Mathematical model

A shell and tube latent heat thermal energy storage (LHTES) unit consists of several wavy tubes, as depicted in Fig. 1 (a). LHTES is filled with a composite copper metal foam and nano-enhanced Coconut oil-CuO. The metal foam is an open foam with a porosity ε where it allows a liquid PCM to move freely between the pores. A hot heat transfer fluid (HTF) with temperature T_h flows inside the tubes and melts the PCM around them. Considering the symmetrical configuration of the tube bundle, one of the tubs can be selected for the unit design, as depicted in Fig. 1 (b). Table 1 list the characteristics of the utilized material. The geometrical configuration of each wavy tube is illustrated in Fig. 1 (c). Here, $L = 200$ mm, and $R_i = 9$ mm. The outer radius of the enclosure was adjusted based on the volume of the wavy tube to provide a constant volume of composite PCM as follows: ($A = 0$ mm, $R_o = 50.4$), ($A = 1$ mm, $R_o = 50.2$ mm), and ($A = 2$ mm, $R_o = 50.11$ mm). The thin copper tube's temperature gradients and transient energy storage were neglected. The parameters of interest are amplitude (*A*) and period of the waves (*N*).

3. Governing equations and boundary conditions

3.1. Convective phase change heat transfer in NEPCM

The molten NEPCM can move between the pores in open metal foams and benefit from natural convection circulations. Thus, the governing equations representing the flow and heat transfer in the composite metal foam-NEPCM are the conservation of mass, momentum, and energy, which can be explained as follows:

I) Mass conservation

$$\frac{1}{r}\frac{\partial(ru_r)}{\partial r} + \frac{\partial u_z}{\partial z} = 0 \tag{1}$$

II) Momentum equations

$$\begin{aligned}&\rho_{\text{NP,l}}\varepsilon^{-2}\left(\varepsilon\frac{\partial u_r}{\partial t} + u_r\frac{\partial u_r}{\partial r} + u_z\frac{\partial u_r}{\partial z}\right)\\ &= -\frac{\partial p}{\partial r} + \frac{\varepsilon^{-1}\mu_{NP,l}}{r}\frac{\partial}{\partial r}\left(r\frac{\partial u_r}{\partial r}\right) - \frac{\varepsilon^{-1}\mu_{NP,l}u_r}{r^2}\\ &+\varepsilon^{-1}\mu_{NP,l}\frac{\partial^2 u_r}{\partial z^2} - \frac{\mu_{NP,l}}{K}u_r + A_{mush}\frac{1-2\omega(T)+\omega^2(T)}{\lambda_e+\omega^3(T)}u_r\end{aligned} \tag{2-a}$$

$$\begin{aligned}&\rho_{\text{NP,l}}\varepsilon^{-2}\left(\varepsilon\frac{\partial u_z}{\partial t} + u_r\frac{\partial u_z}{\partial r} + u_z\frac{\partial u_z}{\partial z}\right)\\ &= -\frac{\partial p}{\partial z} + \frac{\varepsilon^{-1}\mu_{NP,l}}{r}\frac{\partial}{\partial r}\left(r\frac{\partial u_z}{\partial z}\right) + \varepsilon^{-1}\mu_{NP,l}\frac{\partial^2 u_z}{\partial z^2}\\ &+g\rho_{NP,l}\beta_{NP,l}(T-T_{me}) - \frac{\mu_{NP,l}}{K}u_z + A_{mush}\frac{1-2\omega(T)+\omega^2(T)}{\lambda_e+\omega^3(T)}u_z\end{aligned} \tag{2-b}$$

III) Energy conservation

$$\begin{aligned}&(\rho C_p)_{\text{eff,NP}}\frac{\partial T}{\partial t} + (\rho C_p)_{\text{NP,l}}\left(u_r\frac{\partial T}{\partial r} + u_z\frac{\partial T}{\partial z}\right) = \frac{1}{r}\frac{\partial}{\partial r}\left(\lambda_{\text{eff,NP}}r\frac{\partial T}{\partial r}\right)\\ &+\frac{\partial}{\partial z}\left(\lambda_{\text{eff,NP}}\frac{\partial T}{\partial z}\right) - (1-VF_{na})\rho_{\text{PCM,l}}h_{f,\text{PCM}}\varepsilon\frac{\partial\omega(T)}{\partial t}\end{aligned} \tag{3}$$

where the Darcy-Brinkman model was invoked to describe the flow inside the metal foam. Where *u* is the Darcy velocity, *P* is the pressure, and *T* is the temperature field. In the above equations, dynamic viscosity (μ), density (ρ), volume thermal expansion (β), porous permeability (K), the

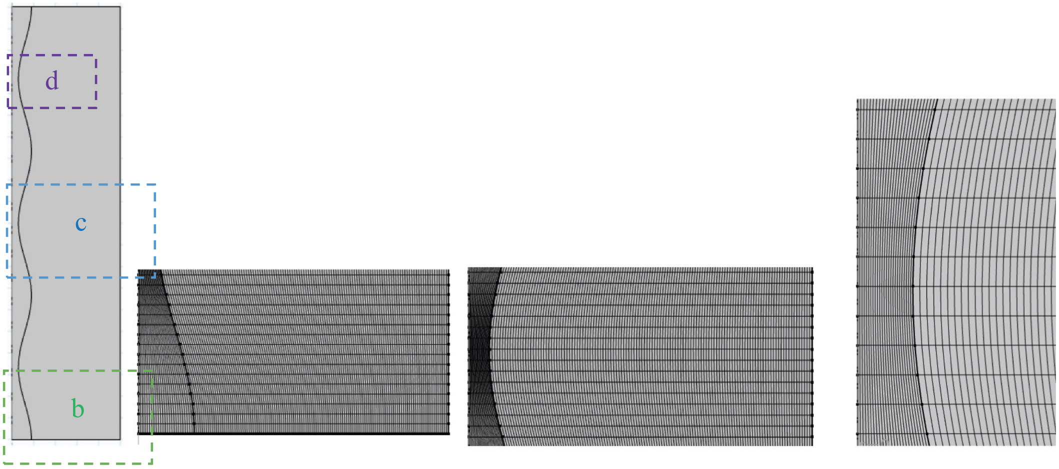

(a) (b) (c) (d)

Fig. 3. A view of adopted mesh with a size of 125 × 125 × 25 for the computational domain.

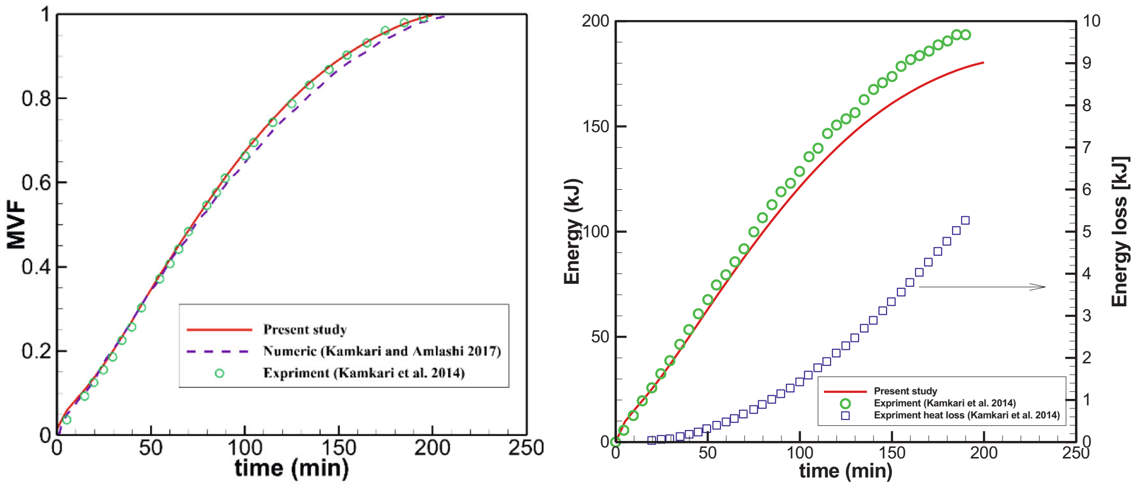

(a) (b)

Fig. 4. A comparison between the results of the present study and the experimental study of [37] and numerical data of [39] for (a) the average melting volume fraction (MVF) and (b) the stored energy in the enclosure.

volume fraction of nanoparticles (VF_{na}), latent heat of fusion (h_f), specific heat capacity (C_p), thermal conductivity (λ), and gravity acceleration constant (g) are the parameters. The subscripts of PCM, na, NP, eff, l, and s indicate the base PCM material, nanoparticles, NEPCM material, effective properties of PCM and metal foam, liquid PCM, and solid PCM, respectively.

In the above equations, the enthalpy-porosity method is employed to model the phase change in the LHTES. In this approach, the phase change takes place in a small temperature range around the fusion temperature of the NEPCM. A phase-field variable, $\omega(T)$, determines the domain with the volume fraction of liquid. A sink term, $A_{mush}[(1-2\omega(T)+\omega^2(T))/(\lambda_e+\omega^3(T))]u)$, is added to the momentum equations, which forces the velocities to zero in solid domains where $\omega = 0$. In the sink term, A_{mush} is a large constant value, 10^{10}, and λ_e is a small number to avoid division to zero. In a solid region, ω tends to be zero, and consequently, the sink term is very large, which forces the velocity to zero. The liquid volume fraction, $\omega(T)$, is introduced around a small temperature range, ΔT_{me} around the NEPCM's fusion temperature, T_{me}, to avoid temperature discontinuities in the heat equation. Here, $\omega(T)$ is defined as:

$$\omega(T)=\begin{cases}0 & T<T_{me}-\Delta T_{me}/2\\ \dfrac{T-T_{me}}{\Delta T_{me}}+\dfrac{1}{2} & T_{me}-\Delta T_{me}/2<T<T_{me}+\Delta T_{me}/2\\ 1 & T>T_{me}+\Delta T_{me}/2\end{cases} \tag{4}$$

In addition, the permeability of the porous domain reads [31]:

$$K=d_p^2\frac{73\times10^{-5}}{(1-\varepsilon)^{0.224}}\left(d_l d_p^{-1}\right)^{-1.11} \tag{5a}$$

$$\left(d_l d_p^{-1}\right)=1.18\left(\frac{1-\varepsilon}{3\pi}\right)^{0.5}\left[1-exp(-(1-\varepsilon)/0.04)\right]^{-1} \tag{5b}$$

In which $d_p = 254\times10^{-4}\omega_p^{-1}$ (*PPI*) where ω_p is the pore per inch characteristics of metal foam (PPI). The effective heat capacity of metal foam and NEPCM is evaluated as:

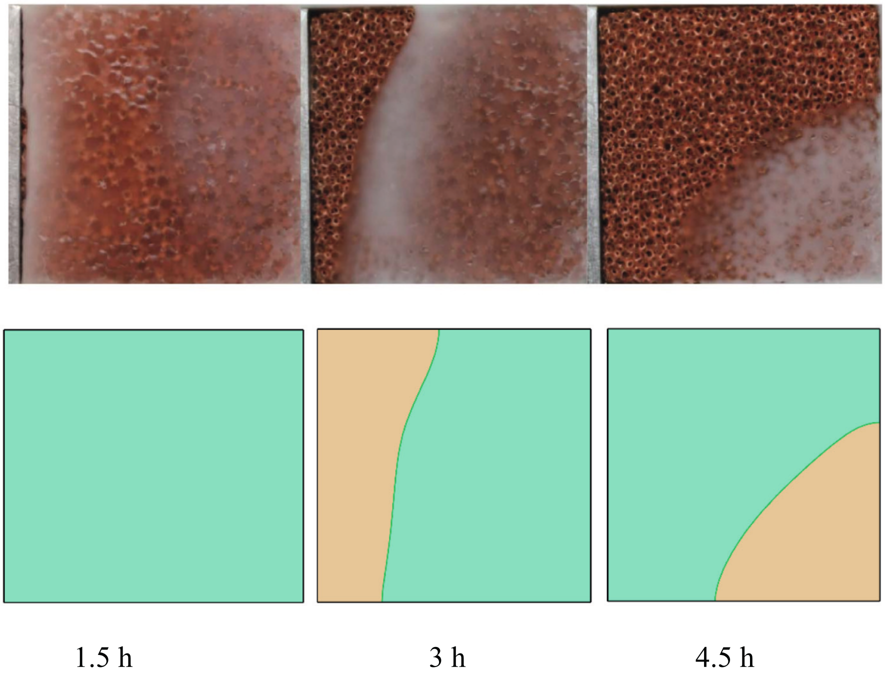

Fig. 5. The empirical observations of [33] and the computed numerical melting interface of the present study.

Table 3
Further investigation on the impact of design parameters around the optimum point.

Case	Parameter	VF_{na}	A (mm)	N	ε	ΔP (Pa)
1	VF_{na}	0	0	4	0.8	0.2
2		0.02	0	4	0.8	0.2
3		0.06	0	4	0.8	0.2
4	A	0.04	1	4	0.8	0.40
5		0.04	2	4	0.8	1.4
6		0.04	3	4	0.8	10.1
7	N	0.04	3	1	0.8	6.5
8		0.04	3	2	0.8	8.3
9		0.04	3	3	0.8	9.4
10		0.04	3	4	0.8	10.1
11	ε	0.04	3	4	0.85	10.1
12		0.04	3	4	0.90	10.1
13		0.04	3	4	0.95	10.1

$$(\rho C_p)_{\mathrm{eff,NP}} = \omega(T)\left[(\rho C_p)_{\mathrm{eff,NP,l}} - (\rho C_p)_{\mathrm{eff,NP,s}}\right] + (\rho C_p)_{\mathrm{eff,NP,s}} \tag{6a}$$

$$(\rho C_p)_{\mathrm{eff,NP,l(s)}} = (1-\varepsilon)(\rho C_p)_{\mathrm{mf}} + \varepsilon(\rho C_p)_{\mathrm{NeP,l(s)}} \tag{6b}$$

Subscript *mf* denotes the solid matrix of the porous medium. Considering the liquid fraction, ω, the thermal conductivity of the composite copper foam-NEPCM is a function of liquid fraction as:

$$\lambda_{\mathrm{eff,NP}} = \omega(T)\lambda_{\mathrm{eff,NP,l}} + (1-\omega(T))\lambda_{\mathrm{eff,NP,s}} \tag{7}$$

The effective thermal conductivity of composite-NEPCM is evaluated utilizing the following relation [32,33]:

$$\lambda_{\mathrm{eff,NP,l(s)}} = \frac{\left[\lambda_{\mathrm{NP,l(s)}} + \pi\left(\sqrt{\chi} - \chi\right)\Delta\lambda_{\mathrm{l(s)}}\right]\left[\lambda_{\mathrm{NP,l(s)}} + (\chi\pi)\Delta\lambda_{\mathrm{l(s)}}\right]}{\lambda_{\mathrm{NP,l(s)}} + \left[\frac{4}{3}\sqrt{\chi}(1-\varepsilon) + \pi\sqrt{\chi} - (1-\varepsilon)\right]\Delta\lambda_{\mathrm{l(s)}}} \tag{8}$$

where $\chi = \frac{1-\varepsilon}{3\pi}, \Delta\lambda_{\mathrm{l(s)}} = \lambda_{\mathrm{mf}} - \lambda_{\mathrm{NP,l(s)}}$.

3.2. *The NEPCM effective properties*

The effective density, thermal expansion, and heat capacity of NEPCM are computed as volume average of PCM and nanoparticles as:

$$\rho_{\mathrm{NP}} = \rho_{\mathrm{PCM}} + VF_{\mathrm{na}}(\rho_{\mathrm{na}} - \rho_{\mathrm{PCM}}) \tag{9a}$$

$$\rho_{\mathrm{PCM}}(T) = \omega(T)(\rho_{\mathrm{PCM,l}} - \rho_{\mathrm{PCM,s}}) + \rho_{\mathrm{PCM,s}} \tag{9b}$$

$$\rho_{\mathrm{NP,l}}\beta_{\mathrm{NP,l}} = \rho_{\mathrm{PCM,l}}\beta_{\mathrm{PCM,l}} + VF_{\mathrm{na}}(\rho_{\mathrm{na}}\beta_{\mathrm{na}} - \rho_{\mathrm{PCM,l}}\beta_{\mathrm{PCM,l}}) \tag{9c}$$

$$(\rho C_p)_{\mathrm{NP}} = \rho_{\mathrm{PCM}}C_{p,\mathrm{PCM}} + VF_{\mathrm{na}}(\rho_{\mathrm{na}}C_{p,\mathrm{na}} - \rho_{\mathrm{PCM}}C_{p,\mathrm{PCM}}) \tag{9d}$$

$$\rho_{\mathrm{PCM}}C_{p,\mathrm{PCM}}(T) = \omega(T)\left[\rho_{PCM,\mathrm{l}}C_{p,PCM,\mathrm{l}} - \rho_{PCM,\mathrm{s}}C_{p,PCM,\mathrm{s}}\right] + \rho_{PCM,\mathrm{s}}C_{p,PCM,\mathrm{s}} \tag{9e}$$

The dynamic viscosity and thermal conductivity of NePCM are evaluated using the Brinkman and the Maxwell equations as:

$$\mu_{\mathrm{NP,l}} = \mu_{\mathrm{PCM,l}}(1 - VF_{\mathrm{na}})^{-2.5} \tag{9f}$$

$$\frac{\lambda_{\mathrm{NP,l(s)}}}{\lambda_{\mathrm{PCM,l(s)}}} = \frac{(\lambda_{na} + 2\lambda_{PCM,\mathrm{l(s)}}) - 2VF_{na}(\lambda_{PCM,\mathrm{l(s)}} - \lambda_{na})}{(\lambda_{na} + 2\lambda_{PCM,\mathrm{l(s)}}) + VF_{na}(\lambda_{PCM,\mathrm{l(s)}} - \lambda_{na})} \tag{9g}$$

3.3. *Forced convection heat transfer inside the tube*

The hot liquid (HTF) enters the wavy tube with a uniform velocity $u_{z,\mathrm{in}}$ and temperature T_h. The governing equations for the forced convection laminar heat transfer in the tube are explained by the conservation of mass, momentum, and energy in a cylindrical coordinate system as follows:

I) Conservation mass

$$\frac{1}{r}\frac{\partial(ru_r)}{\partial r} + \frac{\partial u_z}{\partial z} = 0 \tag{10}$$

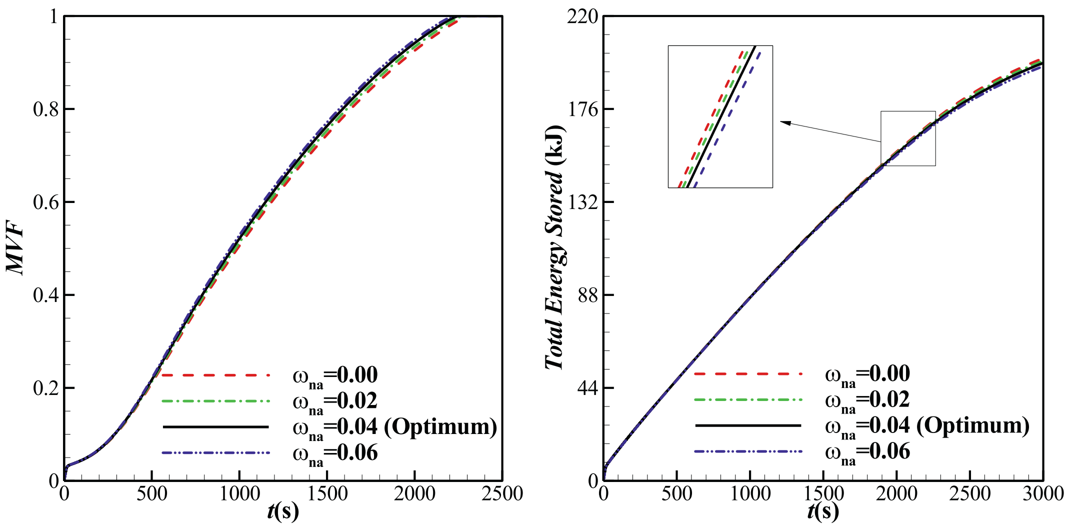

Fig. 6. (a) Melting volume fraction, and (b) Total energy stored as a function of time for different volume fraction (VF_{na} parameter) for case $A = 0$, $N = 4$ and $\varepsilon = 0.8$.

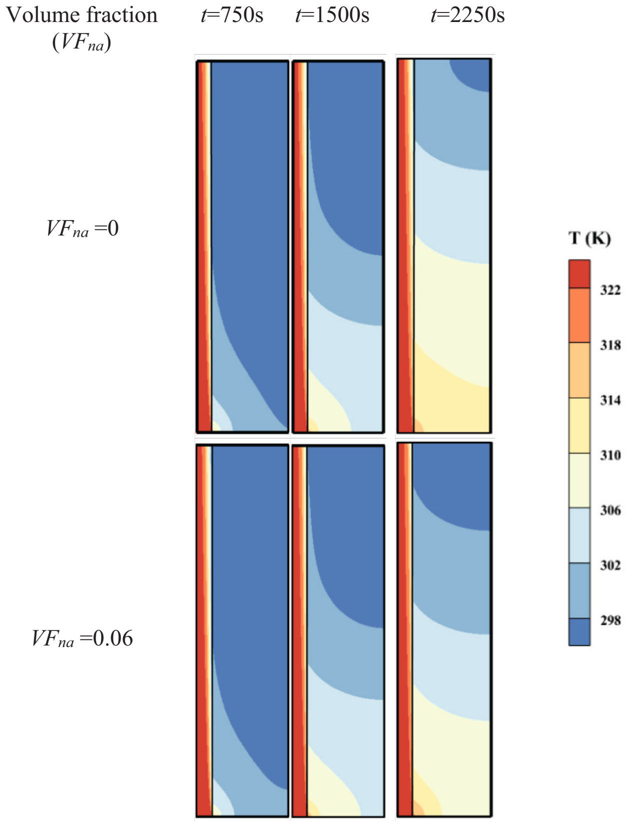

Fig. 7. Impact of volumetric fraction of the nanoparticles on the contours of isotherm, (a) case 1 with $VF_{na} = 0$, and (b) case 3 with $VF_{na} = 0.06$, in three specified times for $A = 0$, $N = 4$ and $\varepsilon = 0.8$.

II) Momentum equations

$$\rho_{\mathrm{HTF}}\left(\frac{\partial u_r}{\partial t}+u_r\frac{\partial u_r}{\partial r}+u_z\frac{\partial u_r}{\partial z}\right) = -\frac{\partial p}{\partial r}+\frac{\mu_{\mathrm{HTF}}}{r}\frac{\partial}{\partial r}\left(r\frac{\partial u_r}{\partial r}\right)-\frac{\mu_{\mathrm{HTF}}u_r}{r^2}+\mu_{\mathrm{HTF}}\frac{\partial^2 u_r}{\partial z^2} \tag{11-a}$$

$$\rho_{\mathrm{HTF}}\left(\frac{\partial u_z}{\partial t}+u_r\frac{\partial u_z}{\partial r}+u_z\frac{\partial u_z}{\partial z}\right) = -\frac{\partial p}{\partial z}+\frac{\mu_{\mathrm{HTF}}}{r}\frac{\partial}{\partial r}\left(r\frac{\partial u_z}{\partial r}\right)+\mu_{\mathrm{HTF}}\frac{\partial^2 u_z}{\partial z^2} \tag{11-b}$$

III) Energy conservation

$$(\rho C_p)_{\mathrm{HTF}}\left(\frac{\partial T}{\partial t}+u_r\frac{\partial T}{\partial r}+u_z\frac{\partial T}{\partial z}\right) = \frac{1}{r}\frac{\partial}{\partial r}\left(\gamma_{HTF}\, r\frac{\partial T}{\partial r}\right)+\frac{\partial}{\partial z}\left(\gamma_{HTF}\frac{\partial T}{\partial z}\right) \tag{12}$$

where subscript HTF indicates the HTF liquid.

3.4. Initial and boundary conditions

Initially, the NEPCM domain and tube are at the initial temperature $T_{initial}$ below the fusion temperature and thus:

$$u_r|_{\mathrm{NP}} = u_z|_{\mathrm{NP}} = 0,\; T|_{\mathrm{NP}} = T_{\mathrm{HTF}} = T_{initial} \tag{13}$$

The HTF enters the tube with a specific uniform hot temperature and velocity

$$T|_{\mathrm{HTF}} = T_h,\; u_r|_{\mathrm{HTF}} = 0,\; u_z|_{\mathrm{HTF}} = u_{z,\mathrm{in}} \tag{14a}$$

and it leaves the tube with a developed convective condition as:

$$u_r|_{\mathrm{HTF}} = 0,\; \left.\frac{\partial T}{\partial z}\right|_{\mathrm{HTF}} = \left.\frac{\partial u_z}{\partial z}\right|_{\mathrm{HTF}} = 0 \tag{14b}$$

The fluid flow in the tube is considered a steady-state, and the steady-state velocity was applied as the initial condition for the HTF flow. For the internal boundary between HTF and metal foam-NEPCM domains, the continuity of heat flux and continuity of temperature were applied as [34,35]:

$$\gamma_{\mathrm{HTF}}\left.\frac{\partial T}{\partial n}\right|_{\mathrm{HTF}} = \gamma_{\mathrm{eff,NP}}\left.\frac{\partial T}{\partial n}\right|_{\mathrm{NP}},\; T|_{\mathrm{HTF}} = T|_{\mathrm{NP}} \tag{14c}$$

where n is normal to surface. The velocity and heat flux at the perimeter of the composite-NEPCM domain is zero as:

$$u_r|_{\mathrm{NP}} = u_z|_{\mathrm{NP}} = 0,\; \left.\frac{\partial T}{\partial z}\right|_{\mathrm{NP}} = 0 \tag{14d}$$

The vertical perimeter was also considered insulated because of the symmetrical placement of the tube bundles. The present model applied the following conditions: $T_{\mathrm{initial}} = 20$ °C, T_h=, 50 °C, and $u_{z,\mathrm{in}} = 0.01$ m/s.

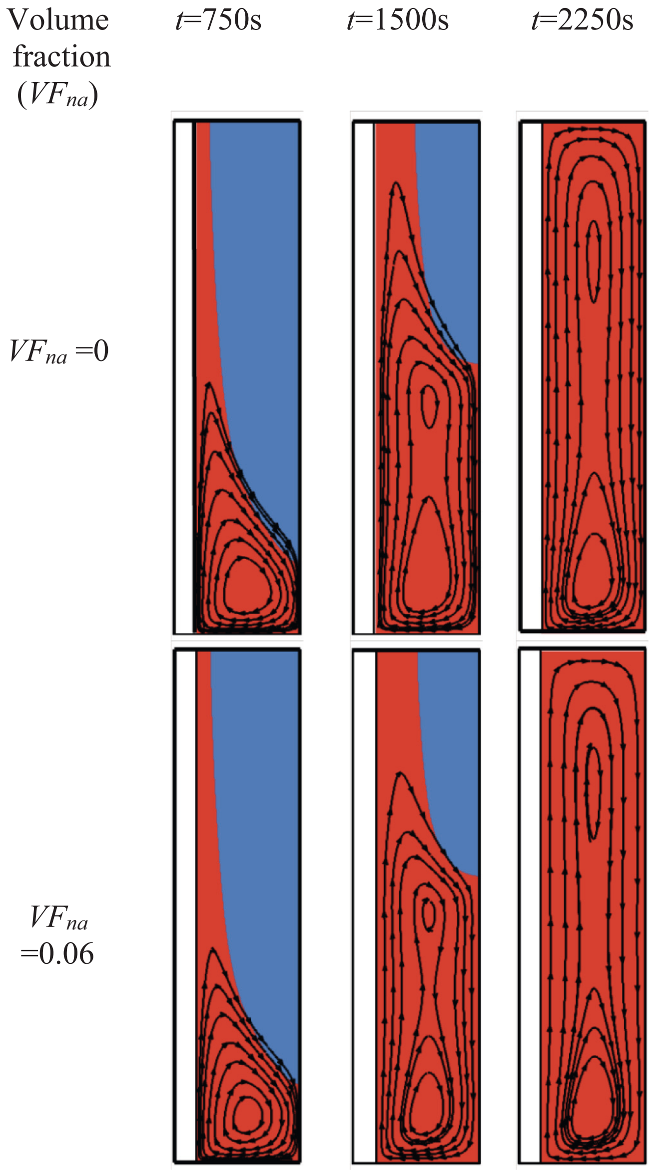

Fig. 8. Imapct of volumetric fraction of the nanoparticles on the streamlines, (a) case 1 with $VF_{\text{na}} = 0$, and (b) case 3 with $VF_{\text{na}} = 0.06$, in three specified times for $A = 0$, $N = 4$ and $\varepsilon = 0.8$.

3.5. Characteristics parameters

The total energy stored in the unit (*ES*), melting volume fraction (*MVF*), and charging power of the unit (*CP*) are the design characteristics and are introduced as follows:

$$ES(t) = \int_V \int_{T_{initial}}^{T} (\rho C_p)_{\text{eff,NP}} dT\, dV + \int_V \omega(T)(1 - VF_{\text{na}})\rho_{\text{PCM,l}}\varepsilon h_{f,\text{PCM}} dV \tag{15}$$

the melting volume fraction is computed as the volume of liquid NEPCM to the overall volume of NEPCM as:

$$MVF(t) = \frac{\int_V \omega(T) dV}{\int_V dV} \tag{16}$$

where the integrations are volumetric integrals due to the axis-symmetric nature of the model. Finally, the thermal energy storage capability of the LHTES unit can be determined by dividing the amount of stored energy by the storage time (full melting time) as:

$$CP = \frac{ES \text{ when the melting process complete}}{\text{complete melting time}} \tag{17}$$

The outlet relative pressure for HTF was zero, so the pressure drop was computed as the average of inlet pressure:

$$\Delta P = \frac{\int_0^{R_i} rpdr}{\int_0^{R_i} rdr} \tag{18}$$

4. Numerical approach and mesh dependency

4.1. Numerical approach

The governing partial differential equations in the HTF and PCM domain were solved using the finite element approach. The momentum and heat equations in the HTF tube and PCM domain were fully coupled with the Newton method's phase change energy equation. A reference pressure-point with a gauge pressure zero was placed at the top left corner of the PCM enclosure as a reference point for the pressure. The momentum and heat equations used the second-order discretization with quadratic shape functions. The equations were solved with a relative error tolerance of 1e-4. The backward differential free step method automatically adjusted the time step and kept the relative error small. More details about the employed method can be found in Ref. [36].

4.2. Mesh study

A non-uniform structured mesh was selected in the HTF and PCM domains. The mesh is uniform on the input, output, and walls, but due to the undulation of the wavy wall, the mesh shrinks or extends inside the computational region. Several mesh sizes (vertical cells × horizontal cells × HTF horizontal cells) were tested when $VF_{\text{na}} = 0.02$, $A = 3$ mm, $N = 3$, and $\varepsilon = 0.85$. The detail of each mesh and computational times are listed in Table 2. The computational time for eight cores, each 2.8 GH and 12 Gb RAM, are also brought in this table.

The average melt volume fraction, MVF, was computed as a function of time and plotted in Fig. 2. As seen, a mesh with a size 125 × 125 × 25 can provide reasonable accuracy with a fair computational cost. Thus, this mesh was selected for computations of the current research. A view of this mesh is illustrated in Fig. 3.

4.3. Model verification

The current numerical code's findings are compared to some literature works to guarantee the correctness and accuracy of the models and calculations. As the first comparison, The current study's results are compared with the experimental results of Kamkari et al. [37] for melting of lauric acid in an enclosure with an initial temperature of 25 °C. The enclosure was a cavity of size 5 cm (width) × 12 cm (height). The cavity walls were well insulated except for one of the vertical walls, which was subject to a constant wall temperature of 70 °C. The volumetric thermal expansion of lauric acid (dodecanol) was adopted as 0.0008 1/K [38], and other thermophysical characteristics of PCM can be found in [37]. Fig. 4 compares the empirical data with the theoretical findings. Fig. 4 (a) demonstrates a high level of concordance between experimental and theoretical data.

Moreover, the empirical stored energy is close to the evaluated theoretical energy storage. There is a gap between empirical stored energy and current data in the final stages of melting. The gap could be due to heat losses. Hence, the empirical energy loss is also plotted in Fig. 4 (b), which increases as time passes. Thus, the results of the present code very well agree with the empirical observations.

Considering the melting heat transfer in metal foams, the current study results are compared with the empirical observations of Zheng

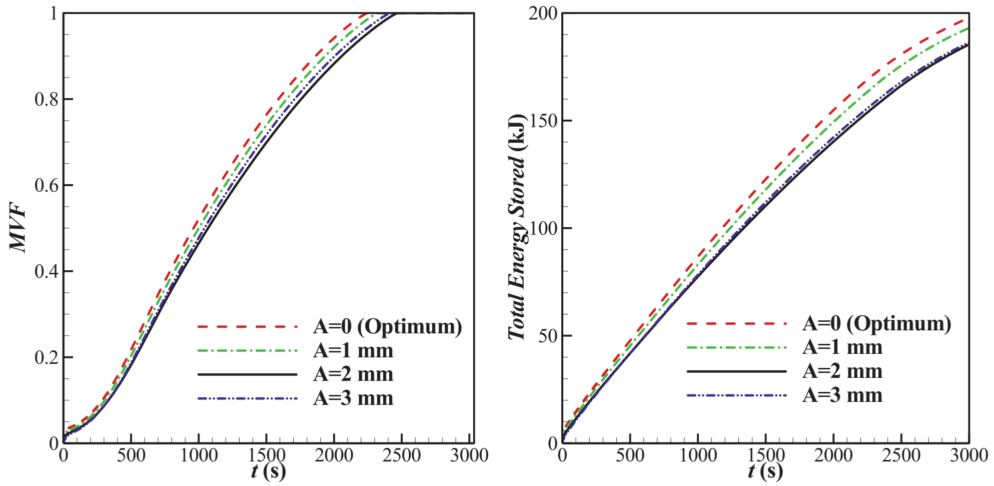

Fig. 9. (a) Melting volume fraction, and (b) Total energy stored as a function of time for different values of wave amplitude (A parameter) for case $VF_{na} = 0.04$, $N = 4$, $\varepsilon = 0.8$.

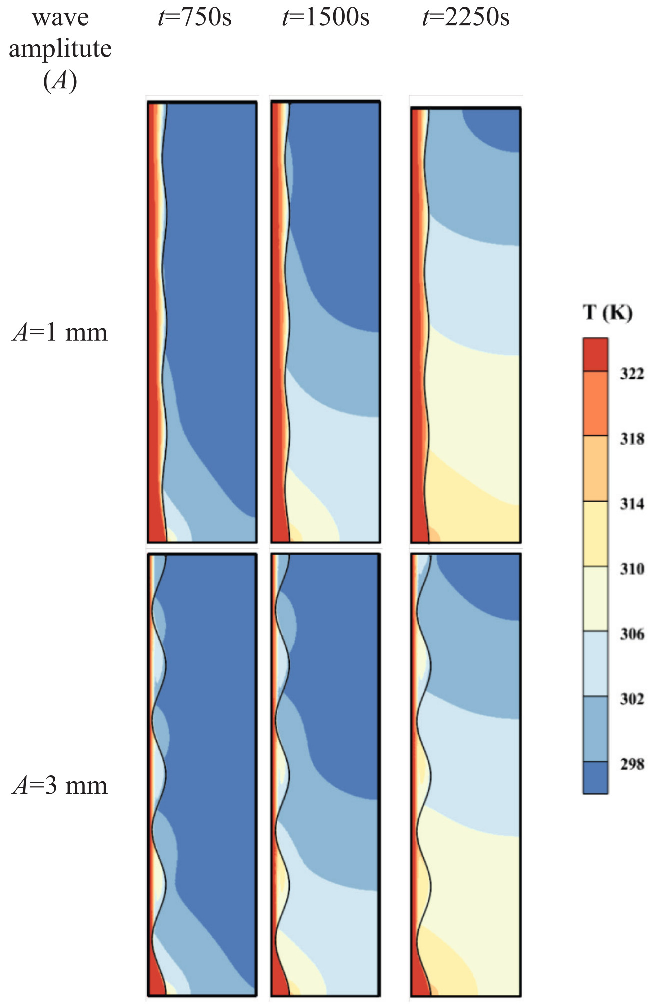

Fig. 10. Impact of wave amplitude (A parameter) on the contours of isotherm, (a) case 4 with $A = 1$ mm, and (b) case 6 with $A = 3$ mm, in three specified times for $VF_{na} = 0.04$, $N = 4$ and $\varepsilon = 0.8$.

et al. [33] for thermal charging of composite paraffin wax copper metal foam. The melting heat transfer was taking place in a cavity of size 10 cm filled with 5PPI copper foam of porosity 0.95. The enclosure walls were subject to no heat transfer except the left vertical wall, which was subject to a heat flux of rate 1150 W/m^2. A small heat loss of 7.5 % was considered. The effective thermal conductivity of the composite and effective latent heat of fusion were 5 W/m K and 132.5 (kJ/kg), respectively [40], while the permeability of the medium was 0.27 mm^2. The remaining thermophysical properties can be found in [33]. As can be observed (See Fig. 5), there is a reasonable agreement between the current investigation's findings and empirical literature works.

5. Results and discussions

The factors of importance in current research are the nanoparticle's concentration ($0 \leq VF_{na} \leq 0.06$), the wave amplitude ($0 \leq A \leq 3$mm), wave period ($1 \leq N \leq 4$), and foam porosity ($0.8 \leq \varepsilon \leq 0.95$). In order to study the influence of each parameter on the melting behavior of PCM in the LHTES unit, here 13 numeric experiments were performed. Table 3 shows the details of each case. Then, the characteristics parameters, contours of melt volume fraction, and temperature distribution are discussed.

The following sections of the present study show the effectiveness of various parameters, including the volumetric fraction of nanoparticles, wave amplitude, number of waves, and porosity coefficient over the melting fraction of the phasing material, the amount of stored energy, constant temperature, and streamlines are investigated.

The impact of waviness on the pressure drop was also investigated in Table 3. As seen, the pressure drop is minimal for a straight channel with no wavy surface (0.2 Pa). A channel with small wave amplitudes also induces a small pressure drop (0.4 Pa). Moreover, as the number of waves increases, the pressure drop also increases. The maximum pressure drop corresponds to the case of $A = 3$ mm and $N = 4$ with $\Delta P = 10.1$ Pa.

5.1. *Volume fraction of nanoparticles*

Fig. 6 (a) and (b) illustrates the procession rate of the melting front and the stored energy for various values of the nanoparticle volume fractions within the time interval of 0 to 2500 s. As can be seen, over time, the curve corresponding to the melting front of the phase change material has been ascending as the entire phase change material is melted in the presence or the absence of nanoparticles after 2500 s. To be more precise, according to Fig. 6 (a), the maximum presence of

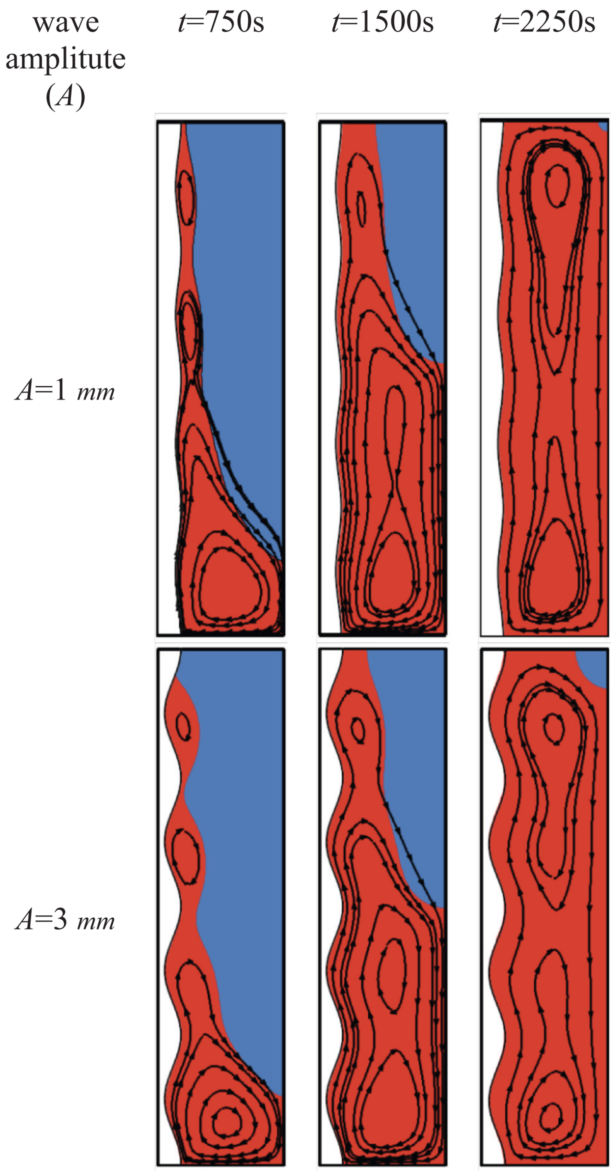

Fig. 11. Effect of wave amplitude (A parameter) on the streamlines, (a) case 4 with $A = 1$ mm, and (b) case 6 with $A = 3$ mm, in three specified times for $VF_{\mathrm{na}} = 0.04$, $N = 4$ and $\varepsilon = 0.8$.

nanoparticles in the phase change material (pure phase change material) has little influence on the progress of the melting front compared to the absence of nanoparticles. The PCM is completely melted in all four curves after about 2200 s. Moreover, the amount of the stored energy decreases as the concentration of nanoparticles increases since nanomaterials do not undergo phase change within the considered temperature range. Nonetheless, the curves in Fig. 7 (a) and (b) oppose each other. Besides, 2000 s after initiation of the melting process, the MVF was computed as 0.925 ($VF_{na} = 0$), 0.934 ($VF_{na} = 0.02$), and 0.948 ($VF_{na} = 0.06$). Thus, using a 6 % concentration of nanoparticles increases the amount of molten NEPCM by 2.5 % compared to a pure PCM.

In the maximum presence of nanoparticles in the phase change material ($VF_{na} = 0.06$), the highest level of melting, and without any nanoparticle ($VF_{na} = 0$), the amount of stored energy is slightly improved. In fact, increasing the volumetric fraction of nanoparticles increases both the thermal conductivity and the dynamic viscosity, enhancing the heat transfer rate and accelerating the melting process. On the other hand, since the latent heat of the nanoparticles is less than the latent heat of the phase change material, the total latent heat of phase change nanomaterial is reduced compared to the pure PCM. Hence, the total energy stored in the absence of nanoparticles is more than in other cases.

In Figs. 7 and 8, constant temperature contours and flow streamlines at three instances of 750, 1500, and 2250-s are evaluated for pure phase change material ($VF_{\mathrm{na}} = 0$), case 1, and phase change nanomaterial with a volume fraction of 0.06 ($VF_{\mathrm{na}} = 0.06$), Case 3. As shown in Fig. 8, excluding the latest time for Case 3, the temperature range is generally within 298 K to 300 K at all three of the time instances, and over time, more areas of the energy storage unit are occupied by higher temperatures. This indicates that the temperature rises in different areas, and the melting front further proceeds. By looking more closely at the constant temperature lines, it can be seen that the patterns obtained in the first two instances (750 and 1500 s) are almost the same for both cases, while in the final time, both the pattern and the range of the temperature for these cases are different. In a way, the lower temperature bond in the first and third cases are equal to 298 K and 302 K, respectively. Following the results obtained in Fig. 8 (a), in the final times, the discrepancy between the curves for $VF_{\mathrm{na}} = 0$ (case 1) and $VF_{\mathrm{na}} = 0.06$ (case 3) has reached the maximum value. In fact, the progress of the melting front depends on the heat transfer rate and the obtained temperature patterns. The largest distance in ending times represents the largest difference between the patterns of constant temperature lines. Hence, at 2250 s, there is a noticeable difference between the constant temperature lines for the first and the third cases. Fig. 8 depicts streamlines at the three-time instances considered before. Streamlines in the molten areas are formed at the bottom of the storage unit and the vicinity of the tube containing hot fluid and have expanded to higher areas as the molten front advances. In the last time, in accordance with Fig. 6 (a), the melting has been completed, and the streamlines are circulating in all areas of the energy storage unit. As mentioned, the origin of streamlines is in the lower areas and adjacent to the pipe containing hot fluid. Therefore, the streamlines are highly packed in these areas for all instances. This is why the strongest circulation currents and, in other words, the highest velocity of the PCM/nanomaterial would occur at the floor of the energy storage unit.

5.2. *Wave amplitude*

The effect of wave amplitude on the melting fraction and the amount of energy stored by the phased change nanomaterial is shown in Fig. 9 (a) and (b). For this purpose, the flat tube ($A = 0$) and the corrugated tube with different wave amplitudes ($A = 0$, 1 mm, 2 mm, and 3 mm) are analyzed. It is worth noting that the area in which the phasing nanomaterial is present remains the same for all four curves. Still, the flat tube area is larger than that of corrugated tubes and decreases with growing wave amplitude. According to the results, both the melting fraction and the amount of energy stored while employing the flat tube are greater than corrugated tubes. However, for the curved tubes, the results are not linear. To clarify, the tube with a wave amplitude of 1 mm has more melting fraction and stored energy than the wave amplitudes of 2 mm and 3 mm, while the 3-mm wave amplitude also reflects better results than the 2-mm one. However, the two curves of the 2- and 3-mm amplitude are very close to each other. In general, corrugation of the pipe is considered an interfering factor for heat transfer from the pipe to the nanomaterial and the circulation of the molten nanomaterial. The increase of the wave amplitude creates both narrow and wide passages on the HTF side. The heat transfer in the HTF side increases at the narrow passages since the local velocity and wall temperature gradients rise. However, it also creates wide passages with minimum flow circulation at the PCM side. The overall heat transfer enhancement is a competition between the increase of heat transfer on the HTF side and the reduction of heat transfer on the PCM side. Thus, no monotonic behavior could be expected. The charging power can be considered as the total stored energy over the required time to store the energy. The charging power at $t = 2000$ s was computed as 78 W (156 kJ/2000 s for

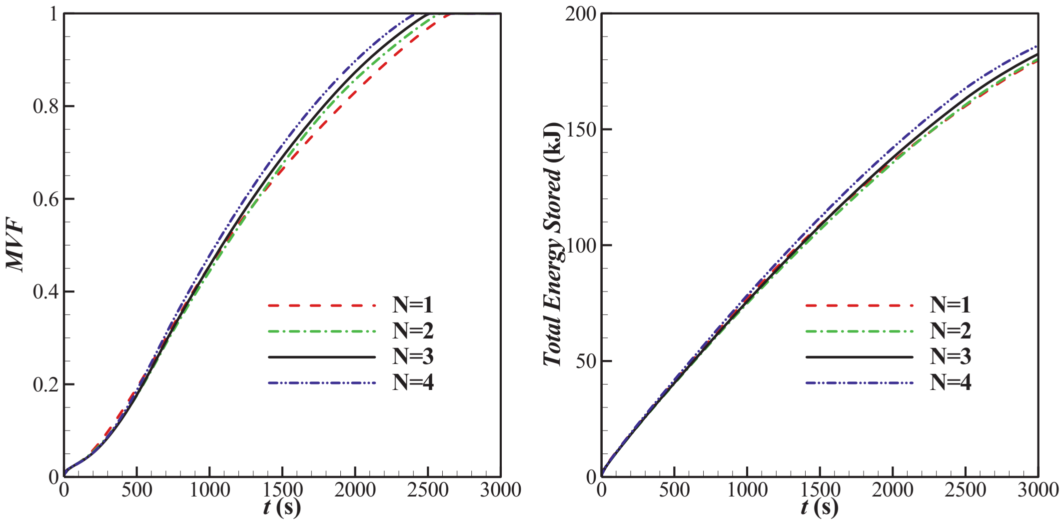

Fig. 12. (a) Melting volume fraction, and (b) Total energy stored as a function of time for various values waves number (*N* parameter) for case $VF_{na} = 0.04$, $A = 3$ mm, $\varepsilon = 0.8$.

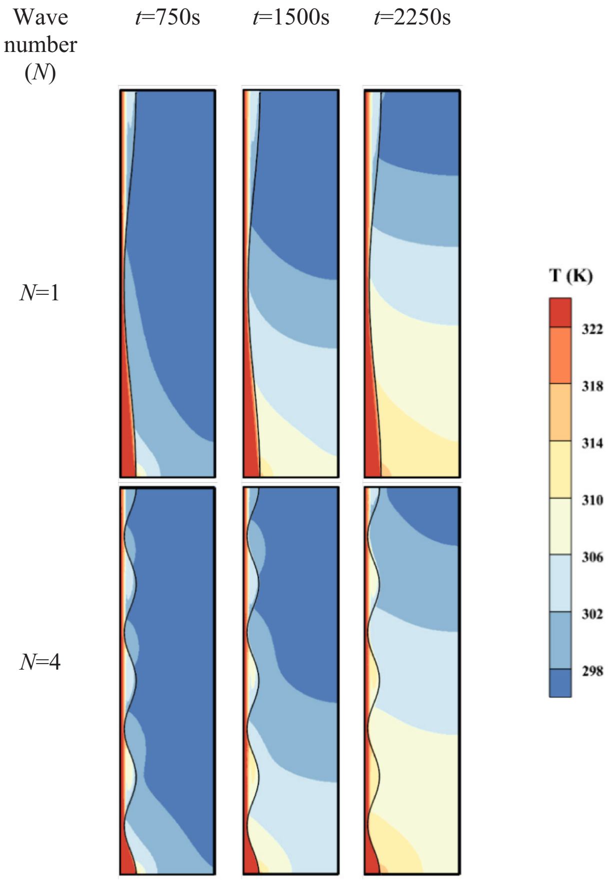

Fig. 13. Impact of waves number (*N* parameter) on the contours of isotherm, (a) case 7 with $N = 1$, and (b) case 10 with $N = 3$, in three specified times for $VF_{na} = 0.04$, $N = 4$ and $\varepsilon = 0.8$.

$A = 0$ mm), 75 W (150 kJ/2000 s for $A = 1$ mm), 70 W (140 kJ/2000 s for $A = 2$ mm), and 71 W (142 kJ/2000 s for $A = 3$ mm). Therefore, case $A = 2$ mm provides about 10 % less power than case $A = 0$ mm.

Figs. 10 and 11 show the constant temperature lines and streamlines of cases 4 (with $A = 1$ mm) and 6 ($A = 3$ mm) in three default time

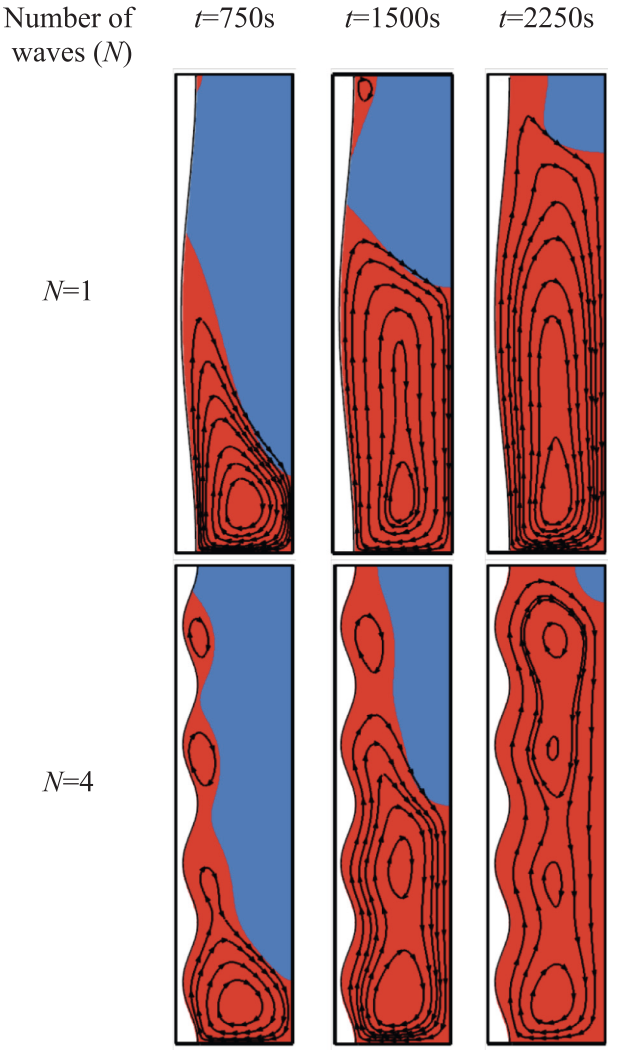

Fig. 14. Effect of number of waves (*N* parameter) on the streamlines, (a) case 7 with $N = 1$, and (b) case 10 with $N = 3$, in three specified times for $VF_{na} = 0.04$, $N = 4$ and $\varepsilon = 0.8$.

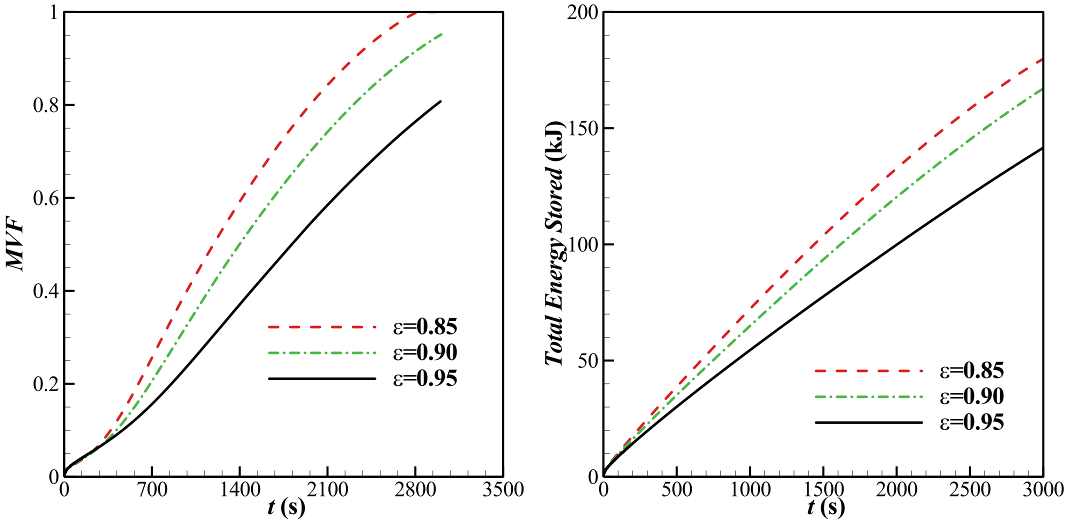

Fig. 15. (a) Melting volume fraction, and (b) Total energy stored as a function of time for different values of porosity (ε parameter) for case $VF_{na} = 0.04$, $A = 3$ mm, $N = 4$.

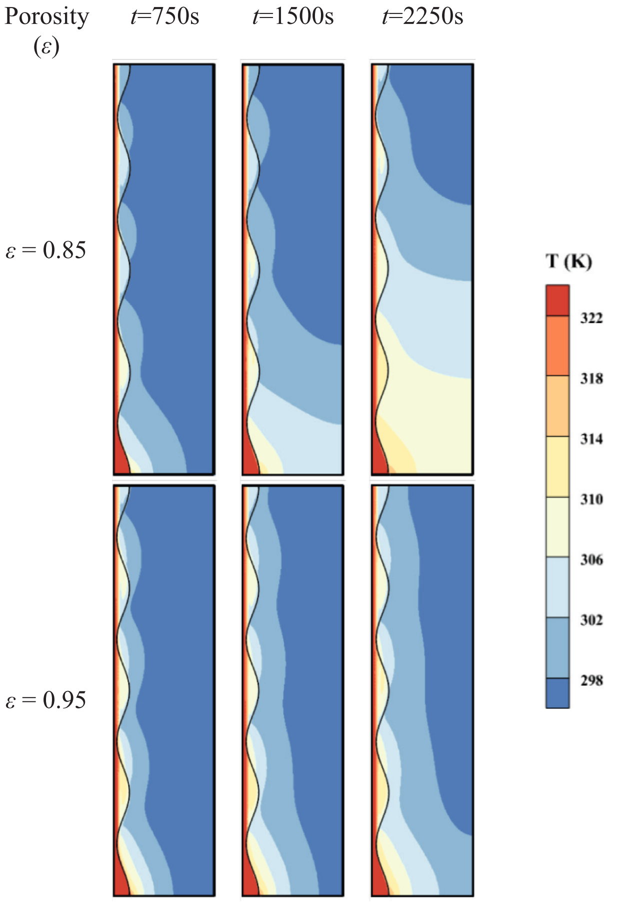

Fig. 16. Effect of porosity (ε parameter) on the contours of isotherm, (a) case 11 with $\varepsilon = 0.85$, and (b) case 13 with $\varepsilon = 0.95$, in three specified times for $VF_{na} = 0.04$, A = 3 mm, and $N = 4$.

instances of 750, 1500, and 2250 s. As can be seen in Fig. 10, at the initial time ($t = 750$ s), the development of the constant temperature lines in the vicinity of wavy surfaces tube with larger amplitude was greater than a wavy tube with smaller amplitude. The lower areas of the chamber are the place of development of the constant temperature lines when wave amplitude is less. Over time, in case 6 with a larger wave amplitude, the patterns of constant temperature lines have a contractionary trend, and their development rate decreases, while the development in the lower areas of the chamber for case 4 with less wave amplitude continues and greater parts of the chamber is occupied by high temperatures.

In accordance with Fig. 10, the flow characteristics of cases 4 and 6 are depicted in Fig. 12. As can be seen, more potent streamlines are initially formed for the larger wave amplitude, but over time, the streamlines associated with the smaller wave amplitude emerges from the lower regions of the chamber and, as a function of the melting front advance, exhibits more development than larger wave amplitudes. Ultimately ($t = 2250$ s), the phase-changing nanomaterial for the smaller wave amplitude reaches the point of almost complete melting. In comparison, the melting process of this material at the larger wave amplitude is not fulfilled.

5.3. Wave number

Fig. 12 exhibits the number of waves of the tube within the default time range and its effect on the melting fraction as well as the amount of stored energy. As can be seen, at primary moments, for the lower wavenumber ($N = 1$), the melting front progress is more than in other cases, although this difference is very small. However, with time and the development of the flow, increasing the number of waves ($N = 4$) leads to the continuous advance of the melting front. In fact, when the number of waves increases, the possibility of developing thermal gradients in the vicinity of the wavy tube at a secondary time is becoming higher, the conduction heat transfer mode is strengthened, and consequently, the melting front advances. Here, the melting process is a comparative function of the boundary-geometric conditions; thus, with the progress of the melting front, the corrugated tube is able to store more energy. It should be noted that the curve of $n = 4$ in these figures is the same curve corresponding to the curve of $A = 3$ mm in Fig. 9. In the previous section, for case 1 with no undulations, the charging power was computed as 78 W at $t = 2000$ s. Considering case 7 with an undulation amplitude of $A = 3$ mm and just one undulation ($N = 1$), the charging power at $t = 2000$ is obtained as 68 W (136 kJ/2000 s). This is while Table 3 shows the pressure drop for Case 1 is just 0.2 Pa while the pressure drop for Case 7 is 6.5 Pa. Thus, an undulation increases the pressure drop and also reduces the charging power. The increase of the wave numbers raises the pressure drop notably and enhances the charging power. By increasing N to 4, the charging power reaches 71 W at $t = 2000$ s, which is still lower

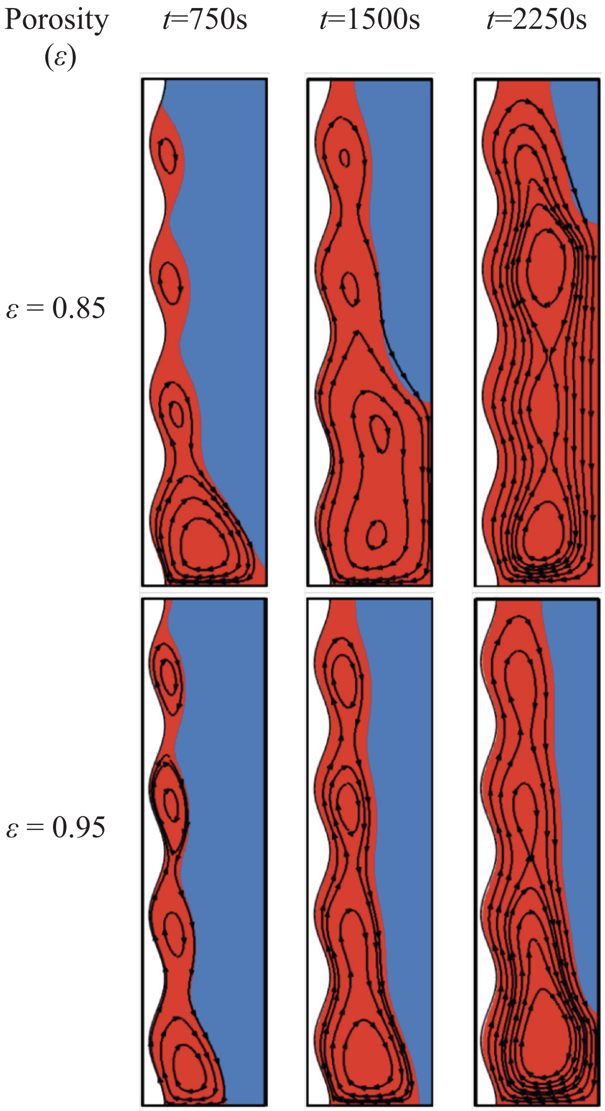

Fig. 17. Impact of porosity (ε parameter) on the streamlines, (a) case 11 with $\varepsilon = 0.85$, and (b) case 13 with $\varepsilon = 0.95$, in three specified times for $VF_{na} = 0.04$, $A = 3$ mm, and $N = 4$.

than the case of a simple tube without waves. Therefore, it can be reckoned that a case (case 1) with flat walls and no wave could result in a higher charging power and lower pressure drop compared to wavy-tube cases.

Constant temperature and streamlines are shown in Figs. 13 and 14 for the lowest and the highest number of waves, $N = 1$ and $N = 4$, at three default time instances. As it is perceptible from Fig. 13, with the increase of the waves number, the spread of temperature lines in the closed chamber (storage source) intensifies, which agrees with the results obtained in Fig. 12. According to Fig. 14, it can also be perceived that for the lowest number of waves, the melting front advances to a greater extent through the lower areas of the chamber, and the formed throat significantly halts the melting of the phase-changing nanomaterial in the upper regions of the chamber. The distribution of the streamlines for a higher wavenumber is more developed, and the melting of mentioned nanomaterial would continue with a greater balance between the lower and upper area of the chamber.

5.4. *Metal foam porosity*

Fig. 15 (a) and (b) shows the influence of the porosity coefficient on the melting fraction of the PCM and the amount of stored energy. As it can be seen, with the growing porosity coefficient parameter, the advance of the melting front decreases, and in the last considered time instance, the phase change material does not completely melt. In general, as the porosity coefficient increases, the porous medium inclines to a simple medium. Therefore, on the one hand, the effect of conduction heat transfer mode is weakened, and on the other hand, convection heat transfer mode prevails. Consequently, the phase change material requires more time to melt through the melting process fully. Increasing the porosity coefficient reduces the contribution of the solid matrix and consequently the thermal conductivity, so the rate of energy stored by the nanomaterial of the phase change declines. Hence, the significance of the porous environment on the performance of phase change processes can be reckoned. It should be noted that the increase of the porosity should increase the overall heat capacity of the enclosure since more NEPCM is available to contribute to the phase change heat transfer. However, here the estimated physical time was 3000 s (along with the fully melted condition); thus, the estimated time was not enough to fully melt the NEPCM for cases $\varepsilon = 0.9$ and $\varepsilon = 0.95$.

Figs. 16 and 17 show the impact of the porosity coefficient on the constant temperature and streamlines at the three default time intervals. According to Fig. 16, the distribution of constant temperature lines for smaller values of the porosity coefficient ($\varepsilon = 0.85$) has increased at all times compared to the high values of this parameter (here $\varepsilon = 0.95$). With further progress of melting front, streamlines for lower values of porosity coefficient compared to higher values are also more developed. Also, following the results obtained in Fig. 16, none of the cases 11 and 13 melted until the last time ($t = 2250$ s).

6. Conclusion

The melting process of the phase change coconut oil containing copper oxide nanoparticles in an energy storage unit in the presence of a wavy tube was evaluated. Hot water passes through the wavy tube and, through satisfying the melting conditions, prompts the melting of the mentioned nanomaterial. The LHTES unit was modeled employing the enthalpy-porosity method and solved using the viable finite element approach. The present fluid dynamics code was compared with previous credible studies. The comparisons demonstrate a reasonable agreement between the current code and the results of prior studies. The independence of the results from the size of the computational grid was analyzed, and the results were extracted according to the size of the selected computational grid. The most substantial results are as follows:

1. By increasing the volumetric fraction of nanoparticles (VF_{na}) within the PCM, on the one hand, the thermal conductivity and dynamic viscosity are improved; thus, the speed of the melting process increases. On the other hand, the thermal capacity of the resulting nanomaterials declines, and the stored energy level would decrease. Also, dispersion of a larger volumetric fraction of nanoparticles within the PCM improves the development of the constant temperature lines, streamlines, and melting front advancement. Using 6 % nanoparticles, increases the melting fraction by 2.5 % after 2000 s.
2. Straight ($A = 0$) and wavy- ($A \neq 0$) tubes with different amplitude sizes were evaluated. Raising the heat transfer level by considering different amplitudes is not a proper option to enhance the melting process and stored energy. As the flat surface tube offers far better results than the wavy tube, the melting front progresses to a greater degree, and the spread of constant temperature and streamlines extends. A wave amplitude of $A = 2$ mm results in minimum charging power (70 W) after 2000 s of charging when $N = 4$. The maximum charging power was 78 W for a simple tube. The pressure drop sharply increased with the increase of the wave amplitude, and the maximum pressure drop was 10.1 Pa for $A = 3$ mm and $N = 4$.
3. The number of tube waves (N) with constant amplitude size was investigated, and its effect on heat-current outputs was determined.

As the number of waves increases, the melting fraction and the amount of energy stored are amplified. Moreover, the increase in the wave number increases the development of constant temperature lines, streamlines, and melting fronts. However, even the results obtained from the maximum number of waves ($N = 4$) cannot boost the mentioned outputs as much as the flat-walled tube. The increase of the wave number increases the pressure drop.

4. The increase in the porosity coefficient (ε), by reducing the solid matrix's share, pushes the porous medium to a simple environment. Therefore, the conduction and convection heat transfer modes are weakened and strengthened, respectively; It takes longer to melt fully, and the level of energy stored diminishes. Furthermore, the distribution of the constant temperature and streamlines deteriorate, and the progress of the melting front in comparison with the lower values of the porosity coefficient decreases.

CRediT authorship contribution statement

M. Ghalambaz: Supervision, Conceptualization, Methodology, Software, Validation, Formal analysis, Data Curation. **A.A. Melaibari:** Visualization, Original draft preparation, Investigation. Formal analysis, Data Curation. **A. J. Chamkha:** Investigation, Writing - Review & Editing. **O. Younis:** Investigation. Formal analysis, Writing - Review & Editing. **M. Sheremet**: Supervision Methodology, Software; Formal analysis, Data Curation.

Declaration of competing interest

The authors clarify that there is no conflict of interest for report.

Data availability

Data will be made available on request.

Acknowledgment

This project was funded by the Deanship of Scientific Research (DSR) at King Abdulaziz University, Jeddah, under grant no. (G: 248-135-1442). The authors, therefore, acknowledge with thanks DSR for technical and financial support.

References

[1] Y. Li, N. Nord, Q. Xiao, T. Tereshchenko, Building heating applications with phase change material: a comprehensive review, J. Energy Storage 31 (2020), 101634.
[2] X. Han, H. Xu, T. Xu, C. Zhao, Magnesium-based thermochemical reactor with multiporous structures for medium-temperature solar applications: transient modelling of discharge capability, Sol. Energy Mater. Sol. Cells 238 (2022), 111630.
[3] D. Li, J. Wang, Y. Ding, H. Yao, Y. Huang, Dynamic thermal management for industrial waste heat recovery based on phase change material thermal storage, Appl. Energy 236 (2019) 1168–1182.
[4] N. Zhang, Y. Yuan, X. Cao, Y. Du, Z. Zhang, Y. Gui, Latent heat thermal energy storage systems with solid–liquid phase change materials: a review, Adv. Eng. Mater. 20 (6) (2018) 1700753.
[5] I. Sarbu, A. Dorca, Review on heat transfer analysis in thermal energy storage using latent heat storage systems and phase change materials, Int. J. Energy Res. 43 (1) (2019) 29–64.
[6] H. Akeiber, P. Nejat, M.Z.A. Majid, M.A. Wahid, F. Jomehzadeh, I.Z. Famileh, J. K. Calautit, B.R. Hughes, S.A. Zaki, A review on phase change material (PCM) for sustainable passive cooling in building envelopes, Renew. Sust. Energ. Rev. 60 (2016) 1470–1497.
[7] K. Du, J. Calautit, Z. Wang, Y. Wu, H. Liu, A review of the applications of phase change materials in cooling, heating and power generation in different temperature ranges, Appl. Energy 220 (2018) 242–273.
[8] S. Wu, T. Yan, Z. Kuai, W. Pan, Thermal conductivity enhancement on phase change materials for thermal energy storage: a review, Energy Storage Mater. 25 (2020) 251–295.
[9] A. Arshad, M. Jabbal, H. Faraji, P. Talebizadehsardari, M.A. Bashir, Y. Yan, Thermal performance of a phase change material-based heat sink in presence of nanoparticles and metal-foam to enhance cooling performance of electronics, J. Energy Storage 48 (2022), 103882.
[10] A. Arshad, M. Jabbal, H. Faraji, P. Talebizadehsardari, M.A. Bashir, Y. Yan, Numerical study of nanocomposite phase change material-based heat sink for the passive cooling of electronic components, Heat Mass Transf. (2021) 1–15.
[11] H. Xu, C. Zhao, Analytical considerations on optimization of cascaded heat transfer process for thermal storage system with principles of thermodynamics, Renew. Energy 132 (2019) 826–845.
[12] N.S. Bondareva, M.A. Sheremet, Effect of the time-dependent volumetric heat flux on heat transfer performance inside a heat sink based on the phase change materials, Clean Technol. Environ. Policy 23 (4) (2021) 1151–1160.
[13] H.M. Al-Najjar, J.M. Mahdi, D.O. Bokov, N.B. Khedher, N.K. Alshammari, M. J. Catalan Opulencia, M.A. Fagiry, W. Yaïci, P. Talebizadehsardari, Improving the melting duration of a PV/PCM system integrated with different metal foam configurations for thermal energy management, Nanomaterials 12 (3) (2022) 423.
[14] M. Esapour, A. Hamzehnezhad, A.A.R. Darzi, M. Jourabian, Melting and solidification of PCM embedded in porous metal foam in horizontal multi-tube heat storage system, Energy Convers. Manag. 171 (2018) 398–410.
[15] H. Xu, Y. Wang, X. Han, Analytical considerations of thermal storage and interface evolution of a PCM with/without porous media, Int. J. Numer. Methods Heat Fluid Flow 30 (1) (2019) 373–400.
[16] P.T. Sardari, D. Grant, D. Giddings, G.S. Walker, M. Gillott, Composite metal foam/PCM energy store design for dwelling space air heating, Energy Convers. Manag. 201 (2019), 112151.
[17] J.M. Mahdi, E.C. Nsofor, Multiple-segment metal foam application in the shell-and-tube PCM thermal energy storage system, J. Energy Storage 20 (2018) 529–541.
[18] H. Xu, L. Gong, S. Huang, M. Xu, Non-equilibrium heat transfer in metal-foam solar collector with no-slip boundary condition, Int. J. Heat Mass Transf. 76 (2014) 357–365.
[19] H. Xu, Z. Qu, W. Tao, Analytical solution of forced convective heat transfer in tubes partially filled with metallic foam using the two-equation model, Int. J. Heat Mass Transf. 54 (17–18) (2011) 3846–3855.
[20] A. Shenoy, M. Sheremet, I. Pop, Convective Flow and Heat Transfer From Wavy Surfaces: Viscous Fluids, Porous Media, and Nanofluids, CRC press, 2016.
[21] M.A. Sheremet, C. Revnic, I. Pop, Free convection in a porous wavy cavity filled with a nanofluid using Buongiorno's mathematical model with thermal dispersion effect, Appl. Math. Comput. 299 (2017) 1–15.
[22] M.A. Sheremet, I. Pop, A. Ishak, Time-dependent natural convection of micropolar fluid in a wavy triangular cavity, Int. J. Heat Mass Transf. 105 (2017) 610–622.
[23] A.I. Alsabery, T. Tayebi, A.J. Chamkha, I. Hashim, Effect of rotating solid cylinder on entropy generation and convective heat transfer in a wavy porous cavity heated from below, Int. Commun. Heat Mass Transfer 95 (2018) 197–209.
[24] A.I. Alsabery, T. Tayebi, A.J. Chamkha, I. Hashim, Natural convection of $$ \mathrm Al _ {2}\mathrm O _ 3 $$ Al 2 O 3-water nanofluid in a non-Darcian wavy porous cavity under the local thermal non-equilibrium condition, Sci. Rep. 10 (1) (2020) 1–22.
[25] F.M. Azizul, A.I. Alsabery, I. Hashim, Heatlines visualisation of mixed convection flow in a wavy heated cavity filled with nanofluids and having an inner solid block, Int. J. Mech. Sci. 175 (2020), 105529.
[26] M. Abdollahzadeh, M. Esmaeilpour, Enhancement of phase change material (PCM) based latent heat storage system with nano fluid and wavy surface, Int. J. Heat Mass Transf. 80 (2015) 376–385.
[27] A. Shahsavar, A. Shaham, P. Talebizadehsardari, Wavy channels triple-tube LHS unit with sinusoidal variable wavelength in charging/discharging mechanism, Int. Commun. Heat Mass Transfer 107 (2019) 93–105.
[28] X. Ma, M. Sheikholeslami, M. Jafaryar, A. Shafee, T. Nguyen-Thoi, Z. Li, Solidification inside a clean energy storage unit utilizing phase change material with copper oxide nanoparticles, J. Clean. Prod. 245 (2020), 118888.
[29] M. Al-Jethelah, S. Ebadi, K. Venkateshwar, S.H. Tasnim, S. Mahmud, A. Dutta, Charging nanoparticle enhanced bio-based PCM in open cell metallic foams: an experimental investigation, Appl. Therm. Eng. 148 (2019) 1029–1042.
[30] S.-K. Choi, S.-O. Kim, T.-H. Lee, Dohee-hahn, computation of the natural convection of nanofluid in a square cavity with homogeneous and nonhomogeneous models, Numer. Heat Transf.; A: Appl. 65 (4) (2014) 287–301.
[31] D.A. Nield, A. Bejan, Convection in Porous Media, Springer, 2006.
[32] O. Mesalhy, K. Lafdi, A. Elgafy, K. Bowman, Numerical study for enhancing the thermal conductivity of phase change material (PCM) storage using high thermal conductivity porous matrix, Energy Convers. Manag. 46 (6) (2005) 847–867.
[33] H. Zheng, C. Wang, Q. Liu, Z. Tian, X. Fan, Thermal performance of copper foam/paraffin composite phase change material, Energy Convers. Manag. 157 (2018) 372–381.
[34] L. Betchen, A.G. Straatman, B.E. Thompson, A nonequilibrium finite-volume model for conjugate fluid/porous/solid domains, Numer. Heat Transf.; A: Appl. 49 (6) (2006) 543–565.
[35] N.H. Saeid, Conjugate natural convection in a porous enclosure sandwiched by finite walls under thermal nonequilibrium conditions, J. Porous Media 11 (3) (2008).
[36] Author Biography, in: O.C. Zienkiewicz, R.L. Taylor, P. Nithiarasu (Eds.), The Finite Element Method for Fluid Dynamics (Seventh Edition), Butterworth-Heinemann, Oxford, 2014, p. ii.
[37] B. Kamkari, H. Shokouhmand, F. Bruno, Experimental investigation of the effect of inclination angle on convection-driven melting of phase change material in a rectangular enclosure, Int. J. Heat Mass Transf. 72 (2014) 186–200.

[38] A.C. Kheirabadi, M. Kabbara, D. Groulx, Geometrical impacts on phase change heat transfer modeling, in: First Pacific Rim Thermal Engineering Conference, 2016.

[39] B. Kamkari, H.J. Amlashi, Numerical simulation and experimental verification of constrained melting of phase change material in inclined rectangular enclosures, Int. Commun. Heat Mass Transfer 88 (2017) 211–219.

[40] X. Xiao, P. Zhang, M. Li, Preparation and thermal characterization of paraffin/metal foam composite phase change material, Appl. Energy 112 (2013) 1357–1366.